A&A 402, 769–780 (2003)
DOI: 10.1051/0004-6361:20030227

Astronomy & Astrophysics

Amplitude and orientation of prominence magnetic fields from constant-α magnetohydrostatic models

G. Aulanier and P. Démoulin

Observatoire de Paris, LESIA, 92195 Meudon Cedex, France
e-mail: guillaume.aulanier@obspm.fr;pascal.demoulin@obspm.fr

Received 27 November 2002 / Accepted 29 January 2003

Abstract. We analyze outputs from three-dimensional models for three observed filaments, which belong to the quiescent, intermediate and plage class respectively. Each model was calculated from a constant-α magnetohydrostatic extrapolation, assuming that the prominence material is located in magnetic dips, so that the field is nearly horizontal throughout the prominence body and feet. We calculate the spatial distribution of the magnetic field amplitude B and orientation θ with respect to the filament axis, neither of which were imposed a priori in the models. In accordance with past magnetic field measurements within prominence bodies, we also obtain nearly homogeneous magnetic fields, respectively of about $B \sim 3, 14$ and 40 G for the quiescent, intermediate and plage prominence, with a systematic weak vertical field gradient of $\partial B/\partial z \sim 0.1{-}1.5 \times 10^{-4}$ G km^{-1}. We also find that the inverse polarity configuration is dominant with $\theta \sim -20°$ to $0°$, which is slightly smaller than in some observations. We also report some other properties, which have either rarely or never been observed. We find at prominence tops some localized normal polarity regions with $\theta < +10°$. At prominence bottoms below 20 Mm in altitude, we find stronger field gradients $\partial B/\partial z \sim 1{-}10 \times 10^{-4}$ G km^{-1} and a wider range of field directions $\theta \sim -90°$ to $0°$. These properties can be interpreted by the perturbation of the prominence flux tube by strong photospheric polarities located in the neighborhood of the prominence. We also report some full portions of prominences that have the normal polarity. The latter are simply due to the local curvature of the filaments with respect to their average axis, which was used to define θ. These results could either be used as predictions for further testing of this class of models with new observations, or as quantitative tools for the interpretation of observations which show complex patterns.

Key words. Sun: prominences – Sun: filaments – Sun: magnetic fields

1. Introduction

Solar prominences consist of long (from 10 to several 100′s of Mm) and thin (1–4 Mm) sheets of cool chromospheric-like plasma, which extend high above the photosphere (10–100 Mm) in the diluted corona. This dense plasma is coupled to highly stressed magnetic fields, which are believed to play a key role in several physical processes within prominences such as the channeling of plasma flows and the maintaining of the prominence plasma at high altitudes for a long time in spite of gravity. It is also believed to drive the sudden eruption of prominences, which are associated with some coronal mass ejections. Therefore, the modeling as well as the direct measurement of prominence magnetic fields have been one of the greatest challenge of solar physics in the past decades (see the book of Tandberg-Hanssen 1995). But this topic still remains unclear due to many difficulties.

On one hand, the direct observation of the vector field within prominences observed at the limb or on the disc requires very high polarimetric accuracy and some spatial resolution (see the reviews of Leroy 1989 and Paletou & Aulanier 2003). Also, the interpretation of such measurements in terms of magnetic field requires complex polarized radiative transfer theories and inversions of Stokes profiles (see e.g. Sahal-Bréchot et al. 1977 for the Hanle effect method and López Ariste & Casini 2002 for the "Principal Component Analysis" method).

On the other hand, the development of appropriate prominence models constitutes a major difficulty (see the review of Démoulin 1998). Firstly the calculated equilibrium configurations should satisfy the MHD equations, with appropriate photospheric boundary conditions, which at least should look like typical magnetograms. Secondly they should qualitatively reproduce typical observational properties, as reviewed for e.g. by Kim (1990), Filippov (1995), Bommier & Leroy (1998), and Martin (1998). Thirdly they must involve strong field-aligned electric currents, since prominence axial fields dominate. This last issue is very sensitive due to theoretical difficulties in calculating such fields, as discussed in the review of McClymont et al. (1997). For all these reasons, prominence models often use several assumptions and/or simplifications. The latter either make the applicability of the model to observations disputable (e.g. two-dimensional models with

Send offprint requests to: G. Aulanier,
e-mail: guillaume.aulanier@obspm.fr

arbitrary axial fields, models involving simplified geometries) or raise the question of their reliability in terms of physics (e.g. constant-α force-free and magnetohydrostatic models) or numerical convergence (e.g. non-linear force-free field models).

Regardless of their assumed degree of reliability, very few prominence models have been analyzed to check their quantitative consistency with specific (or even typical) observations. However, this procedure is clearly needed to identify which models, or theoretical assumptions, are the most satisfactory (see e.g. Anzer 1989; Aulanier & Démoulin 1998; MacKay et al. 2000; Aulanier et al. 2002; Lionello et al. 2002). In parallel, it is clear that recent developments in instrumentation and in interpretation of polarimetric measurements for prominence/filament observations (e.g. Lin et al. 1998; Paletou et al. 2001; López Ariste & Casini 2002; Trujillo Bueno et al. 2002) will soon result in new observations, which should bring further constraints to the modeling.

In this paper we focus on one class of models, based on three-dimensional constant-α (linear) magneto-hydrostatic extrapolations of observed photospheric line-of-sight magnetograms (Low 1992). We analyze the outputs from three of these models, which have been applied in previous publications to specific observations of filaments that belong to the quiescent class (Aulanier et al. 2000, hereafter Paper I), the intermediate class (Aulanier et al. 1999, hereafter Paper II), and the plage class (Aulanier & Schmieder 2002, hereafter Paper III).

The observational context, the models and their limits are described in Sect. 2. In Sects. 3 and 4, we analyze the resulting distribution of the magnetic field amplitude, vertical gradient and orientation within the prominence, which were not explicitly imposed a priori in the models. In Sect. 5 we compare the resulting synthetic scatter plots and maps with past and with more recent measurements. The results are discussed in Sect. 6, with an emphasis on some model predictions that should be tested with new observations.

2. The studied sample of three prominences

In this section we describe what kind of filaments were modeled to produce the present synthetic prominence observations, where they were located and how they were modeled.

2.1. Filaments belonging to different classes

The three studied filaments have been observed on the disc in Hα with various instruments. They belong to different categories, accordingly with the occurence or not of an active region in their vicinity, namely "quiescent", "intermediate" and "plage".

They were all located in the southern hemisphere and they followed the typical hemispheric chirality rules identified by Martin (1998), i.e. sinistral fields and left-bearing feet, the latter being associated with photospheric parasitic polarities.

Their main properties, and the reference to the publications in which they have been studied previously, are summarized in Table 1. Their shape can either be seen in Papers I–III, or on daily full-disc Hα images available on the french solar database BASS2000 (`http://bass2000.obspm.fr/home.php`).

2.2. Summary of the modeling procedure

The models were calculated with the constant-α (linear) magnetohydrostatic extrapolation method (Low 1992), in Cartesian geometry ($\boldsymbol{u}_x$,$\boldsymbol{u}_y$,$\boldsymbol{u}_z$, where z is the altitude), in a periodic computational box in (x; y) of horizontal size L^2 and up to any arbitrary z, by solving the equation

$$\boldsymbol{\nabla} \times \boldsymbol{B} = \alpha \boldsymbol{B} + a \, \exp(-z/H) \, \boldsymbol{\nabla} B_z \times \boldsymbol{u}_z, \quad (1)$$

where α is the "force free parameter", a is a measure of the pressure and gravity induced currents, and H is the scale-height on which these currents decrease with height.

The lower boundary conditions $B_z(z = 0)$ were given by the line-of-sight component of the magnetic field $B_{\|}$ as observed with magnetographs, divided by the cosine of the projection angle (i.e. the so called "radial field approximation"). For the quiescent and the intermediate filament, the magnetogram was modified so as to ensure the appearance of a twisted flux tube for high values of α (as discussed in the Sect. 4.2 of Paper I and Sect. 3.4 of Paper II), whereas the magnetogram was not modified for the plage filament.

The occurence of the prominence within the calculated three-dimensional magnetic field configurations was calculated from the standard assumption (Aulanier & Démoulin 1998) that the prominence plasma rests in equilibrium in the lower portion of magnetic dips within concave field lines, within the first pressure scale-height from the bottom of the dip. The central positions $\boldsymbol{r}_i = (x_i; y_i; z_i)$ of the dips i are given by:

$$(\boldsymbol{B}(\boldsymbol{r}_i) \cdot \boldsymbol{\nabla}) B_z(\boldsymbol{r}_i) > 0, \quad (2)$$

$$B_z(\boldsymbol{r}_i) = 0. \quad (3)$$

In all the models, they are calculated on discretized meshes whose intervals have been chosen so as to obtain a good compromise between keeping a visible separation of individual dips from each other and minimalizing the effects of the discretisation which lead to artificial structures. For various altitudes z, the precise positions $\boldsymbol{r}_i$ satisfying Eq. (3) were found by numerical convergence, using a linear interpolation for $\boldsymbol{B}$ within each interval of the mesh used for the model calculation, then the Eq. (2) criterion was calculated in double precision.

The procedures leading to fix the model parameters (α, a, H, L and when applied, the modification of the photospheric magnetogram) are described in detail in Papers I–III. In brief, the parameters for the intermediate filament were fixed iteratively so as to obtain the best visual fit between the calculated distribution of dips and the Hα filament (Paper II). The parameters for the quiescent filament were guessed from typical observational and theoretical constraints, so that the calculated model was a prediction of the Hα observation (Paper I). Finally the parameters for the plage filament were selected from a grid of 35 calculated models, with the same criteria as for the intermediate filament (Paper III).

The most important model parameters are summarized in Table 1.

Table 1. Observational properties and model parameters for the three filaments analyzed in this study. Papers I–III are respectively Aulanier et al. (2000), Aulanier et al. (1999), and Aulanier & Schmieder (2002).

date of observation	Nov. 04, 1999	Sep. 25, 1996	May 05, 2000
heliographic coordinates	E34 S17	E5 S2	E17 S21
classification	quiescent	intermediate	plage
chirality	sinistral	sinistral	sinistral
Hα observation	BBSO	VTT/MSDP	THEMIS/MSDP
magnetogram	Kitt Peak	SoHO/MDI	SoHO/MDI
(x; y) size L of the box (10^6 m)	266	125	192
α (10^{-8} m^{-1})	+2.34	+4.97	+3.08
α/α(res)	0.99	0.99	0.94
flux tube enforced	yes	yes	no
maximum altitude z of dips (10^6 m)	61	54	34
model published in	Paper I	Paper II	Paper III
figure of the Hα filament	1, *b*	1, *a*	2, *top*
figure of calculated dipped field lines	3, *left*, "$f = 3$"	1, *b*	3, *top*
relevant observed feature	elongated barb	foot F1	elbow
(x; y) coordinates of this feature (10^6 m)	(+30; −60)	(+20; −30)	(−20; +25)
corresponding figure in this paper	Fig. 2	Fig. 3	Fig. 4

2.3. Model orientations and relation with observed features

In each model, the y axis ($x = 0$) was conventionally oriented so as to follow the mean axis of the observed filament, i.e. of the photospheric inversion line of $B_z(z = 0)$ (labeled NL for "neutral line" in Figs. 2–4). The direction of the y axis was set so as to be antiparallel to the mean direction of the calculated prominence axial field, i.e. $< \boldsymbol{B} > \cdot \boldsymbol{u}_y < 0$. Since all the filaments were sinistral, the dominant photospheric polarities $B_z(z = 0) > 0$ (resp. <0) were located at $x > 0$ (resp. <0). These choices are illustrated in Fig. 1.

In order for the reader to be able to relate the shape of the Hα filaments with the color-coded distribution of the central positions of the dips (as viewed from above along the z axis, that are plotted in this paper and described in the next Section), we give in Table 1 the (x; y) coordinates of some specific observed features that were previously described in Papers I–III: the largest foot (also called "barb") of the quiescent and of the intermediate filament, and the elbow of the plage filament, which was also associated with a foot.

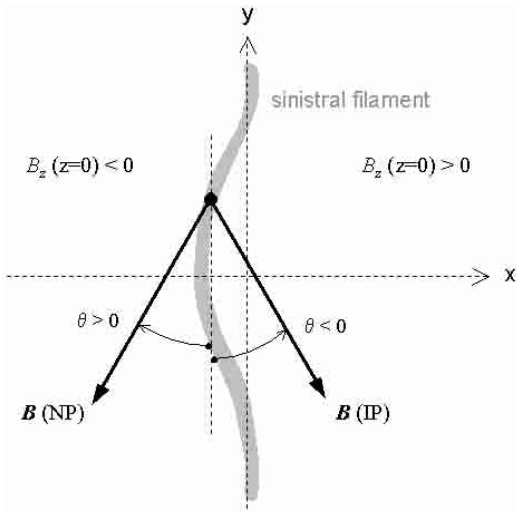

Fig. 1. Definition of the magnetic field orientation angle θ for the modeled sinistral filaments, where the dominant photospheric positive polarities are located in $x > 0$. $\theta < 0$ (resp. >0) and the label IP (resp. NP) correspond to "inverse" (resp. "normal") polarity configurations.

2.4. α and the prominence altitudes

The models were calculated so as to fit the on-disc observations of the Hα filaments only, regardless of their shape as viewed on the limb. The resulting prominence maximum heights were given by the maximum altitude at which magnetic dips were found. In every case the value for the force-free parameter α needed to be higher than 90% of the resonant value, defined as $\alpha(\text{res}) = 2\pi/L$ where L is the size in x and y of the computational box. Therefore the prominence heights were mostly constrained by the amplitude of α.

The resulting height of the intermediate filament, 54 Mm, should be considered with caution. Since it was located almost at disc center, no projection effect could permit to use its apparent altitude as a constraint for α. Also, since the filament feet are mostly due to high-order harmonics of the linear magnetohydrostatic equations (Aulanier & Démoulin 1998), their modeled shape weakly depended on variations of α/α(res) within 0.9–1.

For the quiescent filament, α/α(res) was chosen equal to the one of the former filament, for predictive reasons. But since this filament was located far from disc center and since the prediction matched fairly well the observation, the resulting prominence height of 61 Mm may be considered with good confidence.

The plage filament is the most interesting, because the magnetogram was not modified there to ensure a twisted flux tube, and because it was also located far from disc-center. Since α

was selected among a grid of models with five values in the range $\alpha/\alpha(\mathrm{res}) = 0.88{-}0.98$, the resulting prominence height of 34 Mm is also well defined.

2.5. Limitations of this class of models

In the following we list the most important limitations of constant-α magnetohydrostatic models of prominences, and we discuss their relative importance.

A first limit comes from the validity of the lower boundary conditions used. The assumption that $B_z(z = 0)$ is proportional to the observed $B_{\|}$ can result in errors in the resulting magnetic configurations, especially for the quiescent and plage filaments which were far from disc center. These errors may not be negligible in the vicinity of the weakest photospheric polarities, which can be dominated by transverse fields.

Another limitation comes from the validity of the observed magnetograms, which depend on the spatial resolution, on the instrumental calibrations and on the methods used to deduce magnetic fields from polarimetric observations. For example, Berger & Lites (2002) report a systematic ratio of ~1.4 between the fields measured by the ASP and those measured by MDI. The latter result would imply that every magnetic field value that we calculated for the intermediate and the plage prominence should be multiplied by 1.4 (but this is not incorporated in the values reported in this paper).

Two other limitations come from the periodic treatment in (x; y). The first one is to reduce the amount of flux which overlays the prominence flux tube. About half of the flux contained in the main bipolar component of the photospheric field is connected out of the computational box orthogonally to the filament due to the periodicity in the x direction. The second effect is that the prominence flux tube is not anchored in the photosphere, since it enters and leaves the box along the y axis.

The values for the "force-free parameter" α that are required for the modeled dips to match the observations are very close to the resonant value $\alpha(\mathrm{res})$. This has strong drawbacks. Firstly the prominence flux tube tends to overexpand with height. Secondly the magnetic helicity H_{B} enters into the non-linear branch of the curve $H_{\mathrm{B}}(\alpha)$, calculated by Berger (1985) for constant-α force-free fields. So H_{B} is probably overestimated in the present prominence models, unless one considers its linearized value (as done by Green et al. 2002, for an active region).

In each model, α is constant throughout the whole box. This simplification leads to highly sheared field lines overlaying the prominence flux tube, which do not reproduce the vertical shear gradient identified by Schmieder et al. (1996) in active regions, which is used as the key ingredient of some prominence models (e.g. DeVore & Antiochos 2000). This effect tends to overexpand the whole magnetic configuration with height. This also homogenizes, and possibly underestimates, the twist profile within the prominence flux tube. This last issue is difficult to estimate quantitatively since it would require a systematic comparison with reliable non-constant α extrapolations or realistic coronal MHD evolutions using reliable magnetograms as boundary conditions. Unfortunately such models have only recently begun to be developed, and they also suffer from strong drawbacks such as numerical convergence problems for high α (e.g. Régnier et al. 2002) or they must incorporate strong and ad-hoc electric fields at the photospheric boundary to reproduce the observations (e.g. MacKay et al. 2000; Lionello et al. 2002). Nevertheless, these models are also promising and we believe that they should also be analyzed as in this paper for comparison with each other and with specific observations.

In summary, it is worth remembering that the class of models used in this paper has some limitations that can be disputed and that should be improved. But due to the very good match which were obtained in Papers I–III between the calculated three-dimensional distribution of filled dips and the observed features, we believe that these models provide a good picture of the magnetic field configuration of prominences.

3. Magnetic field amplitudes

3.1. Scatter plots of $\|\boldsymbol{B}\|(z)$

Before analyzing the precise spatial distribution of the magnetic field amplitudes within the modeled prominences, we calculate scatter plots of the vertical distribution of $\boldsymbol{B}$. This permits us to simulate observations as they have been often published (see Sect. 5), where the positions of the measurement points were either uncertain due to projection effects, or averaged in order to enhance the signal to noise ratio.

From the scatter plots of the central position of the dips within the three filaments (Figs. 2–4, top left), two regimes can be defined for each prominence. Considering $h = 20, 15$ and 10 Mm respectively for the quiescent, intermediate and plage prominence, then:

at higher altitude for $z > h$:

- B is nearly homogeneous.

- $\|\boldsymbol{B}\|$ (quiescent) $= 2.5{-}3$ G
- $\|\boldsymbol{B}\|$ (intermediate) $= 13{-}15$ G
- $\|\boldsymbol{B}\|$ (plage) $= 35{-}45$ G

- $\partial B/\partial z$ (quiescent) $\sim +0.1\times10^{-4}$ G km^{-1}
- $\partial B/\partial z$ (intermediate) $\sim +0.3\times10^{-4}$ G km^{-1}
- $\partial B/\partial z$ (plage) $\sim +1.5\times10^{-4}$ G km^{-1}

at lower altitude for $z < h$:

- There is a wide dispersion in B.

- $\|\boldsymbol{B}\|$ (quiescent) $= 0.1{-}4.6$ G
- $\|\boldsymbol{B}\|$ (intermediate) $= 3{-}16$ G
- $\|\boldsymbol{B}\|$ (plage) $= 4{-}60$ G

- $\partial B/\partial z$ (quiescent) $< +1.5\times10^{-4}$ G km^{-1}
- $\partial B/\partial z$ (intermediate) $< +5\times10^{-4}$ G km^{-1}
- $\partial B/\partial z$ (plage) $< +10\times10^{-4}$ G km^{-1}.

The projected maps of the magnetic field within the prominences (see Figs. 2–4, left Col.) show that $z > h$ mostly

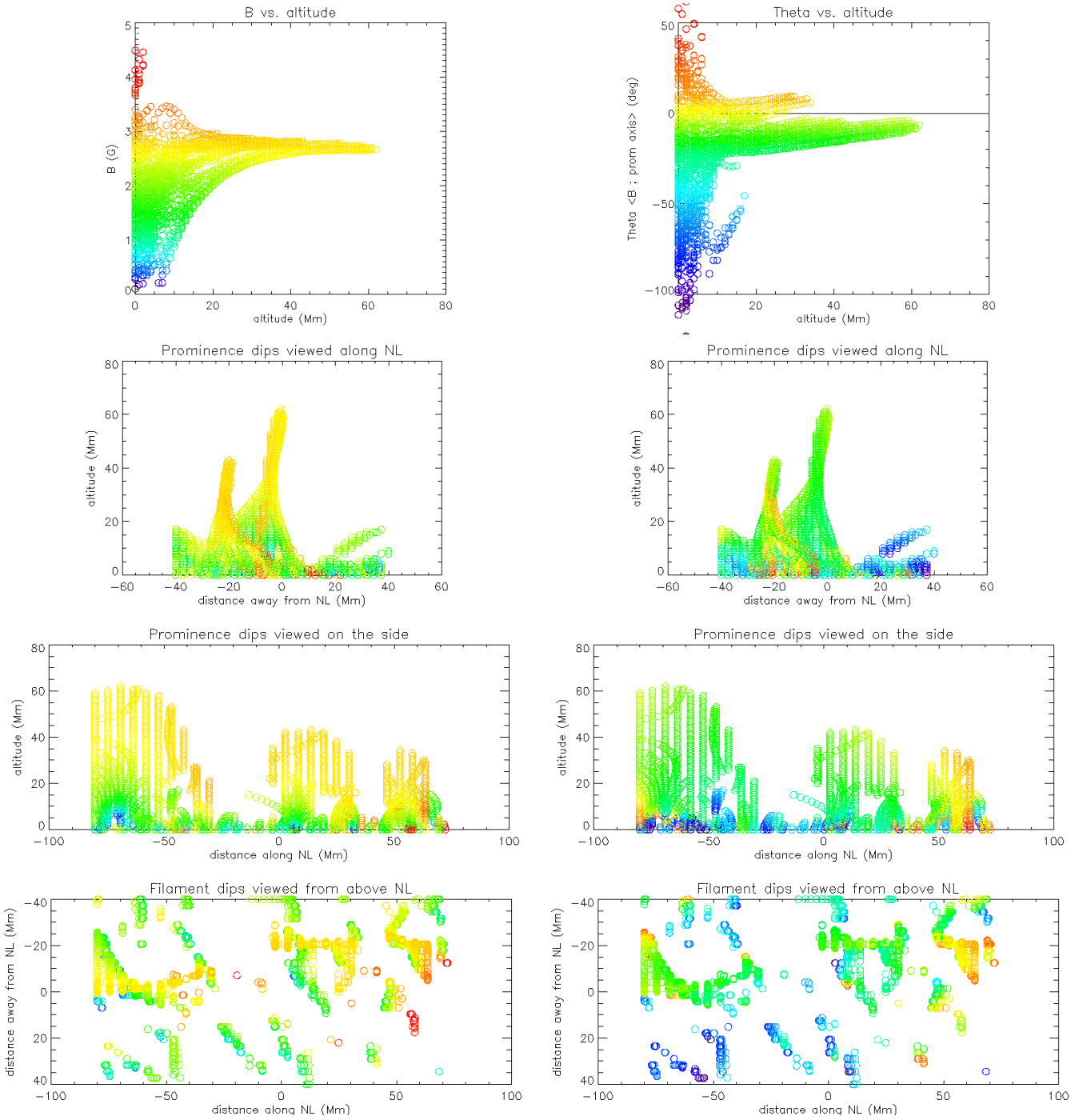

Fig. 2. Color-coded distribution of magnetic dips within the Nov. 04, 1999 quiescent filament, located at E34 S17 (modeled in Aulanier et al. 2000). Only the central position of the dips (i.e. where $B_z = 0$) are shown, as open circles to highlight different structures along the line-of-sight. Left column: amplitude of the magnetic field $\|\boldsymbol{B}\|$. Note that in the prominence body, $< \|\boldsymbol{B}\| > \sim 2.5-3$ G. Right column: angle θ made between $\boldsymbol{B}$ and the mean axis y of the inversion line. $\theta < 0$ (resp. > 0) refer to "inverse" (resp. "normal") polarity fields. Top row: scatter plots of $\|\boldsymbol{B}\|$ and θ versus altitude within the whole prominence. The colors are changing from purple to red as $\|\boldsymbol{B}\|$ and θ increase (for the latter, yellow corresponds to $\theta = 0$); the same color-codes are used in all the panels. Lower rows: 3D projections of the prominence dips (same color-coding as for the top row) as viewed on the limb along the y axis (second row), perpendicularly to the prominence, along the x axis (third row) and from above along the z axis, as for a filament located at disc center (bottom row). Note that the apparent vertical and curved structures within the prominence are an artifact of the discretized calculation of dips.

corresponds to the prominence bodies, which are nearly homogeneous. Therefore the values given above from the scatter plots for $z > h$ do correspond with the ones that can be derived from the maps.

But the same projected maps show that for $z < h$, the prominences are not only composed of their thin vertical body, but also of several feet. The latter form arches below the prominence and they have lateral extensions away from the neutral

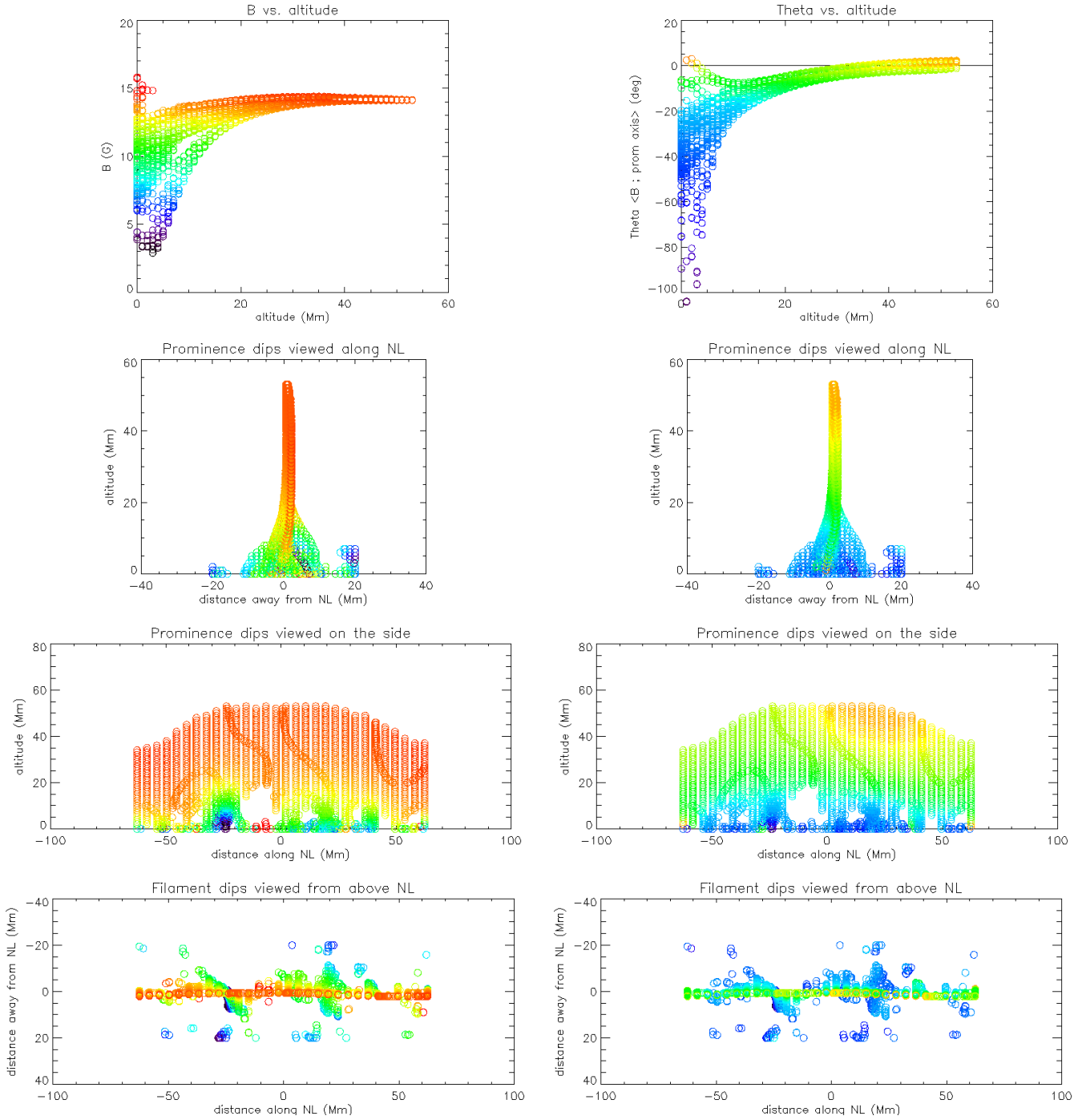

Fig. 3. Same as Fig. 2, but for the Sep. 25, 1996 intermediate filament located at E5 S2 (modeled in Aulanier et al. 1999). Note that $< \|\boldsymbol{B}\| > \sim$ 13−15 G in the prominence body.

line. So for $z < h$, even though the scatter plots are informative, they can lead to several misinterpretations since they incorporate various structures. So we further discuss in Sect. 3.2 the results for $z < h$ by analyzing the magnetic maps.

3.2. Low altitude vertical field gradients

It can be seen on the synthetic maps that the highest vertical field gradients reported in Sect. 3.1 for $z < h$ can in general only been identified if the prominence is viewed on the side (i.e. along x). In particular, they cannot be seen on the models when the prominence is viewed along its axis (y).

Also, the magnetic field amplitudes given in Sect. 3.1 always have their maximum values located at low altitude, being larger than the mean values inside the prominence bodies. This could suggest the existence of negative vertical field gradients for $z < h$. But the magnetic maps clearly show that the highest magnetic fields (in red in Figs. 2–4) are located in specific structures which are not embedded in high altitude weaker

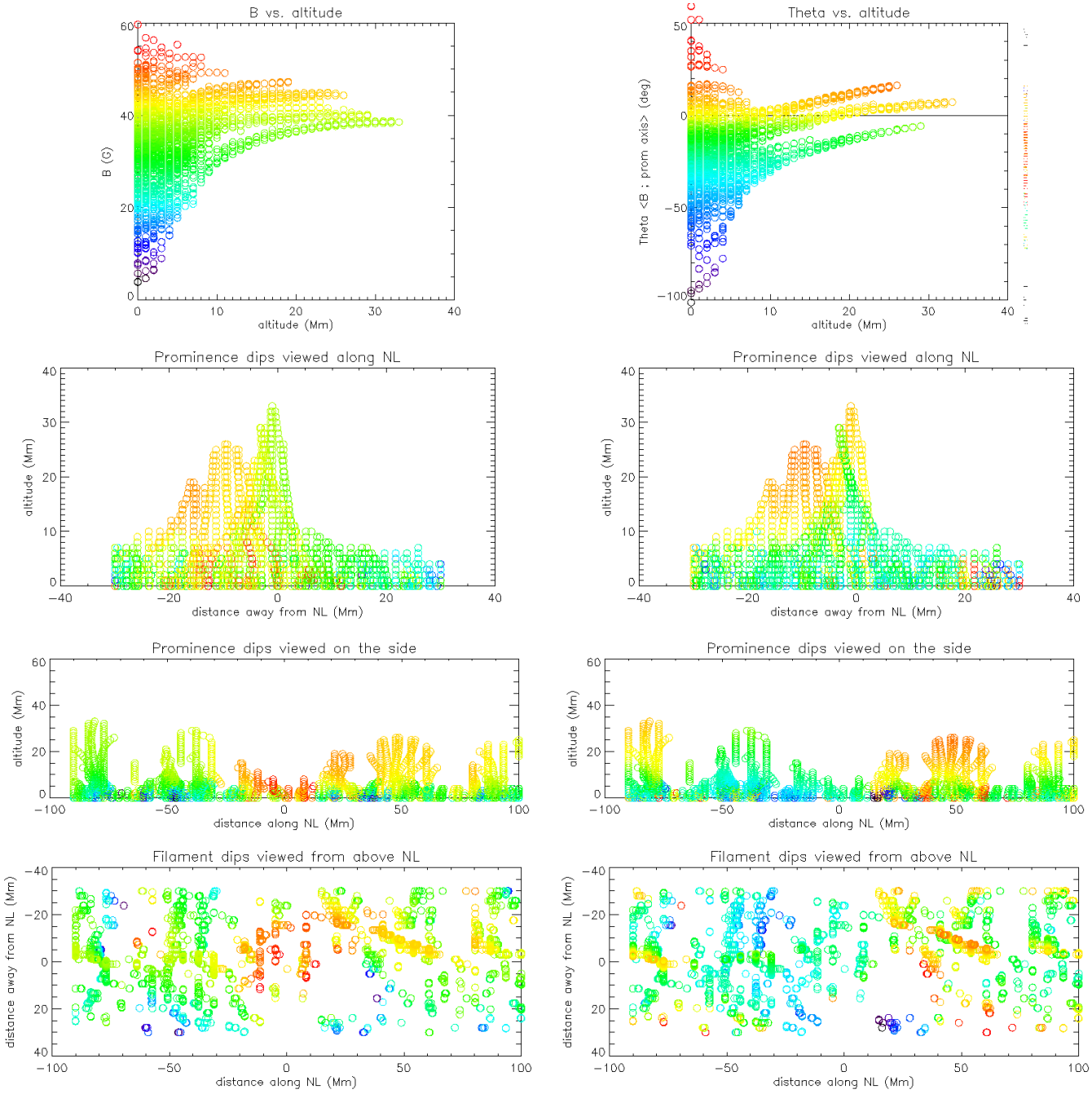

Fig. 4. Same as Fig. 2, but for the May 05, 2000 plage filament located at E17 S21 within a decaying active region (modeled in Aulanier & Schmieder 2002). Note that $< \|\boldsymbol{B}\| > \sim 35{-}45$ G in the prominence body.

field regions, but which are always associated with strong photospheric polarities:

- In the quiescent prominence (Fig. 2) it corresponds to isolated dips located on the edge of the "fragmented barb" (defined in Paper I), far from filament axis at $x \in [+10; +20]$, $y \sim 58$, $z \in [0; +4]$.
- In the intermediate prominence (Fig. 3), this structure is very small, and located right below the prominence body, between two arched feet, at $x \in [-5; +5]$, $y \in [-10; 0]$, $z \in [0; +6]$.
- The plage prominence is the most misleading since the highest field values are located in the prominence body at $x \in [-15; +10]$, $y \in [-12; +12]$, $z \in [0; +15]$. But this portion of the body is not continuous with the rest of the prominence (Fig. 4, left, 3rd row) and it is highly fragmented (Fig. 4, left, bottom row).

In summary, for $(x; y)$ fixed and for $z < h$, the vertical field gradients in the dips calculated from the models are always positive, and even though they can be stronger than for higher altitudes within the prominence bodies (up to a factor 2–3, they

are lower than the maximum values derived from the scatter plots only. The mixing of several independent structures at low altitudes in the scatter plots make them difficult to interpret.

3.3. Prominence shapes and field inhomogeneities

For the class of models used in this paper, the calculated field inhomogeneities within the prominence bodies are a direct function of the ratio between the axial magnetic flux of the prominence flux tube versus the vertical flux of neighboring photospheric polarities, regardless of their "parasitic" (i.e. associated with lateral dips, so prominence feet) or dominant nature. Thus within prominence bodies, the magnetic field inhomogeneities are naturally associated with morphological inhomogeneities such as:

– Long vertical interruptions. They are visible in Figs. 2 and 4 with the views from the side (along x) and from above (along z). The quiescent prominence has two interruptions (see Fig. 2) and the plage prominence is nearly periodically interrupted (see Fig. 4) every ∼20−40 Mm along y, which is the typical size of supergranules.
– The leaning of the prominence. It can occur not only in the (x; y) plane (e.g. the elbow of the plage filament) but also in the (x; z) plane (e.g. the non-vertical body of the quiescent prominence visible in Fig. 2, left, 2nd row). These shifts are due to local changes of the position of the inversion line of B_z at various heights, again due to the effect of neighboring photospheric polarities.

These models imply that the effects described above may lead to several difficulties in interpreting off-limb magnetic field measurements, since the photospheric polarities cannot be observed simultaneously. This becomes even more difficult for prominences observed along their mean axis, since several prominence parts will overlap in the observing plane (e.g. as in Casini & López Ariste 2003), while the magnetic field can differ significantly in these parts.

4. Magnetic field orientations

4.1. Definition of the orientation angle θ

In the following, $\theta \in [-\pi; +\pi]$ has been defined as the angle made by the magnetic field vector $\boldsymbol{B}$ (only in the central positions of the dips, so that $B_z = 0$) and the y axis. $\theta < 0$ (resp. >0) and $B_x > 0$ (resp. <0) corresponds to the inverse (resp. normal) polarity configuration, hereafter called IP (resp. NP) as shown in Fig. 1. This definition for θ was chosen so as to follow the same procedure as in many previously published papers on prominence magnetic field measurements. So when the filament axis is curved, θ does not correspond to the angle between the magnetic field vector and the local direction of the filament axis.

4.2. Scatter plots of $\theta(z)$

As for the magnetic field amplitudes, two regimes can be identified from the scatter plots of θ, depending on the altitude h as defined in Sect. 3.1:

at higher altitude for $z > h$:

- IP dominates with $-20^\circ < \theta$ and $< \theta > \sim -10^\circ$
- a few NP exist with $\theta < +20^\circ$ and $< \theta > \sim +5^\circ$

at lower altitude for $z < h$:

- IP dominates with $-90^\circ < \theta$ and $< \theta > \sim -40^\circ$
- some NP exist with $\theta < +50^\circ$.

The IP is dominant for high altitudes. But θ is only weakly negative. This is natural since the prominence flux tube is weakly twisted in the models. The IP is also dominant at low altitudes since for every model, the flux tube often reaches the $z = 0$ photospheric plane. The existence of normal polarity (NP) regions, not only at low altitudes but also within the prominence bodies, is not intuitive for this kind of models based on twisted flux tubes (Aulanier et al. 2002). Two specific types of NPs are described and interpreted in Sects. 4.3 and 4.4.

4.3. "Curvature related" NP fields

The first kind of NP which appears in the models covers large fractions of some sections of prominence bodies, that are often isolated by some long vertical interruptions mentioned in Sect. 3.3. These NP regions can be directly visualized in Figs. 2 and 4 (left Col.) with the yellow and red colors. One of these NP regions is visible in the quiescent prominence and three are present in the plage filament.

This kind of NP is readily explained by the definition of θ, which only uses the mean prominence axis for reference (see Sect. 4.1 and Fig. 1). In fact, it can be shown that these NP fields are almost all IP with respect to the local filament axis. So, these NP dips are just due to the curvature of the filament axis, and therefore are not "true" NP. This can occur either at low altitude due to neighboring magnetic concentrations on the photosphere, or more globally due to inhomogeneities in the photospheric bipolar background which do not smooth fast enough at larger altitudes (see Aulanier & Démoulin 1998 for analytical proofs under the linear force-free field approximation).

The latter situation is obviously important for the plage filament, since it was located between two decaying active regions and since the magnetogram was not modified to calculate the model.

4.4. "Photospheric polarities related" NP fields

Another kind of NP area is present for the intermediate filament at large heights (Fig. 3, right Col.). On one hand, according to Aulanier et al. (2002), the present NP fields are not an intrinsic property of prominence models based on twisted flux tubes, such as the ones studied in this paper. On the other hand,

some photospheric polarities are present in the vicinity of these NP (in x and y), which form lateral dips (labeled S2 and S3 in Fig. 1 of Paper II) and which slightly modify the orientation of the filament at lower altitude (see the Fig. 2 of Paper II). But for this prominence, these polarities have a negligible effect on the orientation of the prominence at large altitude (as explained in Sect. 3.3). Therefore these NP dips cannot be of the same type as those reported in Sect. 4.3. They are true local NP configurations.

Indeed, these NP dips find their origin in the three-dimensional perturbation of the central part of the twisted flux tube at $z \sim z_c$ (i.e. at the prominence top) by some photospheric polarities that have a net horizontal field $B_x(z) < 0$. Even though their negative B_x decreases with height much faster than the horizontal field of the twisted flux tube, it dominates at the tube center, since the unperturbed flux tube has $B_x(z_c) = 0$. So a NP region can be formed around $z = z_c$.

In fact this effect does not occur everywhere in our prominence models, in spite of numerous photospheric polarities described in Papers I–III. This is due to the fact that in order to produce a NP dip (not only a NP region), the criterion given by Eqs. (2) and (3) must also be satisfied. So under some circumstances, the formation of the NP region may also destroy the dip, resulting in the absence of NP within the prominence. In particular, NP dips can never be formed in 2.5-D globally bipolar configurations invariant in the y direction, because a dip (Eq. (2) with $\partial/\partial y = 0$) implies that B_x must be of the same sign as $\partial B_z/\partial x$.

5. Comparison with past measurements

In this section, we compare the present models of three specific observed filaments with past observations of several other prominences. Note that the magnetic field amplitudes and orientations within prominences were not explicitly imposed in the models a priori.

Note also that due to instrumental limitations (e.g. use of a coronograph or presence of stray light near the solar limb), most of prominence observations were done for high altitude prominences, and typically for $z > 10$ Mm. So the comparisons of our models with the observations are mostly restricted to the regime $z > h$ defined in Sects. 3.1 and 4.2.

We recall that we only considered the magnetic field in the central part of each prominence dip. Further analysis shows that with the present models, an average along the dip region does not lead to significant changes. So on the one hand, we can compare the results of our models with observations, both with optically thin lines (which give an average of the field in the prominence) as well as with optically thick lines (which give the field at the edge of the prominence), if several groups of dips are not integrated along the line-of-sight. But on the other hand, the issue of radiative transfer will have to be addressed in more detail for low altitude regions (where several feet can overlap) or when the prominence is observed along its axis (as discussed in Sect. 3.2). Note finally that our results could be modified if some very dense plasma could be trapped in the dips, if the plasma β is of the order or greater than one. The gravity would then modify the magnetic field locally, as in the local models of magnetic dips by Heinzel & Anzer (2001). Since the precise values of β in prominence are not well established, this debated issue will have to be investigated in the future.

5.1. Amplitudes

Magnetic field amplitudes were first obtained for the longitudinal component only, using the Zeeman effect. The measured values were typically $B_{\|} \sim 5{-}60$ G (Rust 1967), $B_{\|} \sim 3{-}8$ G (Tandberg-Hanssen 1970; Tandberg-Hanssen & Anzer 1970), $B_{\|} \sim 5{-}25$ G (Nikolsky et al. 1982, 1984; Kim 1990; Bashkirtsev & Mashnich 1998).

The amplitude of the vector field was then measured from linear polarization analyzed with the Hanle effect theory (Sahal-Bréchot et al. 1977). Such measurements were done for quiescent prominences, $1/3$ being located in the polar crown and $2/3$ being located in medium and low latitudes, not excluding plage regions The reported values are $B \sim 1{-}10$ G (Leroy 1977), $B \sim 2{-}15$ G (Leroy et al. 1983; Bommier et al. 1994), $B \sim 3{-}30$ G (Athay et al. 1983) and $B \sim 6{-}60$ G (Querfeld et al. 1985). More recent observations analyzed with the "anisotropic radiation pumping effect", taking into account lower-level atomic polarization, result in $B \sim 20{-}40$ G (Trujillo Bueno et al. 2002).

Leroy et al. (1984) reported that magnetic fields are statistically weaker for high altitude (quiescent) prominences, of the order of $B \sim 1{-}5$ G, and stronger for lower altitude prominences, of the order of $B \sim 10{-}20$ G. Also, the highest values $B > 30$ G are extremely rare, but this may be due to the systematic selection of the lowest field intensity in the Hanle diagrams, when multiple solutions co-existed (Bommier, private communication). It is worth noticing that recent full spectro-polarimetric observations (Paletou et al. 2001) analyzed with the "Principal Component Analysis" (PCA) method (López Ariste & Casini 2002) have given $B \sim 40{-}60$ G. Interestingly, the same observations analyzed with the linear polarization only (as done with the Hanle effect measurements) resulted in $B \sim 20$ G only.

The modeled amplitudes of $B(z > h)$ given in Sect. 3.1 are fully consistent with the observed values (even with taking into account the underestimation of the field by SoHO/MDI as measured by Berger & Lites 2002). They also reproduce the lower (resp. stronger) fields for quiescent (resp. intermediate) prominences. The modeled fields in the plage prominence are higher than the most frequent values obtained with the Zeeman and Hanle methods, but still fall in the observed ranges. They are also compatible with the recent simultaneous analyses of full spectro-polarimetric observations that take into account the linear and circular polarization.

5.2. Horizontal fields

The magnetic field measurements with the Hanle effect resulted in magnetic field vectors being nearly parallel with the photosphere, i.e. horizontal fields. This has been measured e.g. by Leroy (1978), Athay et al. (1983), Bommier et al. (1986),

Bommier et al. (1994) and more recently by López Ariste & Casini (2002).

The synthetic scatter plots and magnetic maps produced in this study were calculated at the central position of magnetic dips. So the observed horizontality of prominence magnetic fields is naturally reproduced by the present models (Aulanier & Démoulin 1998) but also by all the prominence models which are based on magnetic dips (reviewed in Démoulin 1998).

Moreover, as noted in Aulanier & Démoulin (1998) and in Papers I–III, these models also predict that the magnetic field is also dipped, so mostly horizontal, within prominence feet (also called barbs). When the feet reach the photosphere, they form "bald patches" (i.e. portions of inversion lines where the field vector is tangent to the photosphere, see Titov et al. 1993).

5.3. Vertical gradients

Some of the authors listed in Sect. 5.1 measured vertical gradients of the magnetic field, either using the longitudinal Zeeman effect or the Hanle effect. The reported values are $\partial B_{\|}/\partial z \sim 10^{-4}$ G km^{-1} (Rust 1967), $\partial B_{\|}/\partial z \sim 0.5 \times 10^{-4}$ G km^{-1} (Nikolsky et al. 1984), $\partial B_{\|}/\partial z \sim 1 - 10 \times 10^{-4}$ G km^{-1} (Bashkirtsev & Mashnich 1998), $\partial B/\partial z \sim 0.6{-}1.6 \times 10^{-4}$ G km^{-1} (Leroy 1977), $\partial B/\partial z \sim 0$ (Athay et al. 1983), $\partial B/\partial z \sim 0.5 \times 10^{-4}$ G km^{-1} (Leroy et al. 1983). A striking result is that all these gradients are positive. The different values may be attributed to the fact that the measurements were done for different type of prominences, but also that they were not always done for fixed positions in $(x; y)$, and that they suffer from uncertainties due to some observational and theoretical difficulties (see Leroy 1989).

Even though these measurements may be disputed, we recall that such positive gradients are equivalent to the presence of magnetic dips. This has been demonstrated by Anzer (1969) for magnetic dips created by gravity acting on initially undipped potential fields and by Démoulin & Priest (1989) for force-free fields. It is then natural than the models analyzed in this paper also result in $\partial B/\partial z > 0$. Interestingly, the modeled gradients given in Sect. 3.1 fall in the range of the observed values for $z > h$. Also, as in the observations, we report apparent negative gradients which appear when $\partial B/\partial z$ is not calculated at $(x; y)$ fixed (see Sect. 3.2).

The magnetic field for $z > h$ is mostly dominated by the twisted flux tube, which mainly depends on the large-scale photospheric bipolar background and on the treatment of the force-free parameter α. So it seems that the model approximations that concern α (see Sect. 2.5) can be a posteriori justified.

The modeled gradients for $z < h$ given by the models are larger than the observed values reported above (apart from Bashkirtsev & Mashnich 1998), which were all measured at higher altitude in prominence bodies. This issue will need to be clarified by new measurements at low altitudes, close to solar limb.

5.4. Orientations

The orientation angle θ of the horizontal vector field with respect to prominence axis derived from observations has been, and still is, a debated issue among observers, essentially due the well known "180° ambiguity" in the direction of the transverse field (perpendicularly to the line of sight). This ambiguity often permits to find two distinct physical solutions within prominences: the normal polarity (NP) and the inverse polarity (IP).

Before Leroy et al. (1983), even though the IP configuration was sometimes explicitly mentioned (e.g. Leroy 1977), the NP case was always chosen by default since it corresponds to "classical" potential (or sheared, but not sigmoidal) field lines. With this method, the observers found $|\theta| \sim 0{-}20°$ in low altitude prominences within active regions, $|\theta| \sim 10{-}40°$ in quiescent and polar crown prominences, and $|\theta| \sim 0{-}90°$ in plage prominences located between active regions (Tandberg-Hanssen & Anzer 1970; Leroy 1978; Querfeld et al. 1985).

The history and the various methods which have been used to get rid of the 180° ambiguity are given in the reviews of Démoulin (1998) and Bommier & Leroy (1998). For 256 prominences, Leroy et al. (1984) statistically measured $\theta = -25° \pm 40°$ (the total dispersion being wider than the value given here, which corresponds to 1σ), with 75% of IP prominences. For 14 prominences in which the 180° ambiguity has been individually solved, Bommier et al. (1994) reported $\theta = -35° \pm 15°$ (at 1σ), with 85% of IP prominences. Finally, for 296 prominences, Bommier & Leroy (1998) obtained $\theta = -40° \pm 30°$ (at 1σ), with more than 90% of prominences being IP. These results suggest that a great majority of prominences are either fully IP, or are dominated by IP fields.

Regarding the nature of the NP cases, Leroy et al. (1984) statistically associated them with lower altitude, bright and sharp-edged prominences (with a maximum height of ∼30 Mm). The plage prominences probably fall in this class: for e.g. the 2 NP prominences observed by Bommier et al. (1994) were located in the vicinity of an active region. Unfortunately, the spatial distribution of the NP regions were not studied since the reported B and θ values were always averaged from every measured positions, in order to enhance the polarimetric accuracy (Bommier, private communication). Also, their sample was biased towards the higher prominences and the higher parts of prominences because of the occulting disk of their coronograph.

Two independent studies (with the longitudinal Zeeman effect only), by Nikolsky et al. (1982, 1984) and Bashkirtsev & Mashnich (1998), reproduced the same result, but also suggested the occurence of mixtures of IP and NP within a few intermediate prominences. Unfortunately the latter measurements are unclear since only one component of the magnetic field was measured.

Since the models conclude that prominences are formed in moderately twisted flux tubes, they naturally reproduce the IP configuration within the prominences bodies, as well as characteristic chromospheric "fishbone" features firstly noted by Filippov (1995). As shown in Figs. 2 and 3, the tendency to have smaller $|\theta|$ in the intermediate prominence than in the

quiescent prominence is also reproduced. Quantitatively, the modeled values for $|\theta|(z > h)$ are typically lower by a factor 2 than the mean observed values. This may be associated with the difficulty of constant-α models to produce highly twisted configurations (see Sect. 2.5). The values for $|\theta|(z < h)$ are larger, so closer to the typically observed ones.

The occurence of extended regions of NP dips in the models (see Sects. 4.2 and 4.3) is in agreement with the observations of Nikolsky et al. (1984), and may be associated with the low altitude prominences of Leroy et al. (1984). This issue certainly needs to be addressed in more details with new observations.

Finally it is worth emphasizing that observations should have as little spatial overlap as possible between different prominence parts, in order to get a better diagnosis of individual structures. Thus, observations from the side of the prominence (as in Figs. 2–4, third row) are recommended.

6. Conclusion

In this paper we analyzed outputs from three-dimensional prominence models, based on magnetic dips and calculated with the constant-α magnetohydrostatic extrapolation method. This method was initially developed by Low (1992) for active regions, and it was first used to model filaments, in Aulanier et al. (1999), Aulanier et al. (2000) and Aulanier & Schmieder (2002). Each of these three modeled filaments were observed on the disc in Hα and interestingly, each fell in a different class: quiescent, intermediate and plage. The objective of the present paper was to analyze the models in the frame of magnetic field measurements within prominences, which had not been done in the related publications.

The models result in nearly homogeneous magnetic fields within filament bodies, of $B \sim 3, 14$ and 40 G in the quiescent, intermediate and plage prominence respectively. In accordance with the dip hypothesis, weak vertical field gradients are obtained. Their typical values range in $\partial B/\partial z \sim 0.1{-}1.5 \times 10^{-4}$ G km^{-1}. As a consequence of the resulting weakly twisted flux tube topology, the modeled configurations are dominated by inverse polarity (IP) dips, with mean angles between the field vector and the prominence axis of $\theta \sim -20^{\circ}$ to 0°. We have shown in Sect. 5 that these modeled values match with the measured ones with surprisingly good accuracy.

These new results, combined with the good fit which was obtained between the observed shape of Hα (and EUV) filaments and the calculated lower portions of the dipped field lines (described in the related publications), as well as with the natural reproduction of the hemispheric chirality rules depending on the sign of the force-free parameter α (Aulanier & Démoulin 1998), suggest a posteriori that the major hypotheses and approximations of this class of models are at first order justified. In particular the constant-α hypothesis does not seem as restrictive as intuitively supposed.

Moreover, the models produce some extended normal polarity (NP) regions, which we separated into two types. The first one corresponds to NP regions that cover almost every altitude of some subsections of a prominence body. We interpreted them as being due to local curvatures of the prominence axis, the latter being due to large scale field inhomogeneities in the photosphere. The models show that these apparent NP are in fact IP when the orientation angle is not calculated with respect to the mean axis of the prominence, but rather to its local axis. The second type NP regions are true NP. They are less extended and they are located at prominence tops. We have shown that they correspond to the perturbation of the central axis of the prominence twisted flux tube, by the coronal response to photospheric polarities that have a net horizontal field such as to produce NP regions where the prominence magnetic field is nearly aligned with its axis, i.e. at the prominence tops. We discussed in Sect. 5 how these properties may fit the NP cases observed by Leroy et al. (1984), Nikolsky et al. (1984) and Bashkirtsev & Mashnich (1998). But we believe that such conclusions are not yet convincing, so that new measurements of the distribution of NPs within the same prominence should be done, for further comparison with the models.

To the authors' knowledge, the only other prominence model that predicts mixtures of IP and NP dips is the "sheared arcade model" (DeVore & Antiochos 2000). In this model the NP dips are due to the effect of the differentially sheared arcades which are dipped by the downward magnetic tension from the overlaying potential fields (Aulanier et al. 2002). Even though these NP dips are physically different than the ones reported in this paper, it may not be evident to distinguish the two cases in observations, especially if we take into account that the observed photospheric field distribution is more complex than in this idealized model. So we argue that the "sheared arcade versus twisted flux tube" testing procedure that has been proposed by Aulanier et al. (2002) may not be straightforward if mixtures of NPs and IPs are observed in the future.

The models used in this paper show that the occurence of small photospheric polarities in the vicinity of the prominence cause noticeable perturbations (not only at low altitude in the feet but also at various heights) such as inhomogeneities in morphology, field amplitude and orientation. These effects constitute quantitative predictions that could be tested with new prominence magnetic field measurements at every altitude and observing the same prominence on the disc and at the limb. The model predictions are (i) horizontal magnetic fields, IP configurations and bald patches in the feet, (ii) stronger vertical field gradients at low altitude (typically $z < 15$ Mm), up to a factor 10, (iii) magnetic field inhomogeneities and deviations from verticality of the prominence body, both being associated with large scale photospheric inhomogeneities, and (iv) the formation of true NP regions at prominence tops, due to the net horizontal component of small scale photospheric polarities.

In the future it would also be interesting to compare different models analyzed as in this paper, in order to derive their specific or relative properties. It would be particularly interesting to compare models of one same filament calculated with different methods that use observed magnetograms as lower boundary conditions (e.g. the intermediate filament modeled in this paper was also modeled by Lionello et al. 2002 with a MHD simulation). The next step would be to compare models of a given filament with magnetic field measurements of the same object, as viewed on the disc and at the limb, in the latter case assuming that the magnetic field configuration does not change during the transit on the disc.

Acknowledgements. We wish to thank V. Bommier, J.-L. Leroy, A. López Ariste, S. Koutchmy and F. Paletou for valuable discussions about prominence magnetic field measurements and for their input in the writing of Sect. 5.

References

Anzer, U. 1969, Sol. Phys., 8, 37
Anzer, U. 1989, in Dynamics and Structure of Quiescent Solar Prominences, ed. E. R. Priest (Dordrecht: Kluwer), 143
Athay, R. G., Querfeld, C. W., Smartt, R. N., Degl'Innocenti, E. L., & Bommier, V. 1983, Sol. Phys., 89, 3
Aulanier, G., & Démoulin, P. 1998, A&A, 329, 1125
Aulanier, G., Démoulin, P., Mein, N., et al. 1999, A&A, 432, 867 (Paper II)
Aulanier, G., Srivastava, N., & Martin, S. F. 2000, ApJ, 543, 447 (Paper I)
Aulanier, G., & Schmieder, B. 2002, A&A, 386, 1106 (Paper III)
Aulanier, G., DeVore, C. R, & Antiochos, S. K. 2002, ApJ, 567, L97
Bashkirtsev, V. S., & Mashnich, G. P. 1998, in New Perspectives on Solar Prominences, IAU Colloq. 167, ed. D. Webb, B. Schmieder, & D. Rust, ASP Conf. Ser., 150, 90
Berger, M. A. 1985, ApJS, 59, 433
Berger, T. E., & Lites, B. W. 2002, Sol. Phys., submitted
Bommier, V., Leroy, J.-L., & Sahal-Bréchot, S. 1986, A&A, 156, 79
Bommier, V., Landi Degl'Innocenti, E., Leroy, J.-L., & Sahal-Bréchot, S. 1994, Sol. Phys., 154, 231
Bommier, V., & Leroy, J.-L. 1998, in New Perspectives on Solar Prominences, IAU Colloq. 167, ed. D. Webb, B. Schmieder, & D. Rust, ASP Conf. Ser., 150, 434
Casini, R., & López Ariste, A. 2003, in Third workshop on solar polarization, ed. J. Trujillo Bueno, & J. Sánchez Almeida, ASP Conf. Ser., in press
Démoulin, P. 1998, in New Perspectives on Solar Prominences, IAU Colloq. 167, ed. D. Webb, B. Schmieder, & D. Rust, ASP Conf. Ser., 150, 78
Démoulin, P., & Priest, E. R. 1989, A&A, 214, 360
DeVore, C. R., & Antiochos, S. K. 2000, ApJ, 539, 954
Filippov, B. 1995, A&A, 303, 242
Green, L. M., López Fuentes, M. C., Mandrini, C. H., et al. 2002, Sol. Phys., 208, 43
Heinzel, P., & Anzer, U. 2001, A&A, 375, 1082
Kim, I. S. 1990, in Dynamics of Quiescent Prominences, ed. V. Ruždjak, & E. Tandberg-Hanssen (New York: Springer), 49
Leroy, J.-L. 1977, A&A, 60, 79
Leroy, J.-L. 1978, A&A, 64, 247
Leroy, J.-L. 1989, in Dynamics and Structure of Quiescent Solar Prominences, ed. E. R. Priest (Dordrecht: Kluwer), 77
Leroy, J.-L., Bommier, V., & Sahal-Bréchot, S. 1983, Sol. Phys., 83, 135
Leroy, J.-L., Bommier, V., & Sahal-Bréchot, S. 1984, A&A, 131, 33
Lin, H., Penn, M. J., & Kuhn, J. R. 1998, ApJ, 493, 978
Lionello, R., Mikić, Z., Linker, J. A., & Amari, T. 2002, ApJ, 581, 718
López Ariste, A., & Casini, R. 2002, ApJ, 575, 529
Low, B. C. 1992, ApJ, 399, 300
MacKay, D. H., Gaizauskas, V., & van Ballegooijen, A. A. 2000, ApJ, 544, 1122
Martin, S. F. 1998, Sol. Phys., 182, 107
McClymont, A. N., Jiao, L., & Mikić, Z. 1997, Sol. Phys., 174, 191
Nikolsky, G. M., Kim, I. S., & Koutchmy, S. 1982, Sol. Phys., 81, 81
Nikolsky, G. M., Kim, I. S., Koutchmy, S., & Stellmacher, G. 1984, A&A, 140, 112
Paletou, F., & Aulanier, G. 2003, in Current Theoretical Models and High Resolution Solar Observations: Preparing for ATST, ASP Conf. Ser., 286, 45
Paletou, F., López Ariste, A., Bommier, V., & Semel, M. 2001, A&A, 375, L39
Querfeld, C. W., House, L. L., Smartt, R. N., Bommier, V., & Degl'Innocenti, E. L. 1985, Sol. Phys., 96, 277
Régnier, S., Amari, T., & Kersalé, E. 2002, A&A, 392, 1119
Rust, D. M. 1967, ApJ, 150, 313
Sahal-Bréchot, S., Bommier, V., & Leroy, J. L. 1977, A&A, 59, 223
Schmieder, B., Démoulin, P., Aulanier, G., & Golub, L. 1996, ApJ, 467, 881
Tandberg-Hanssen, E. 1970, Sol. Phys., 15, 359
Tandberg-Hanssen, E. 1995, The Nature of Solar Prominences (Dordrecht: Kluwer)
Tandberg-Hanssen, E., & Anzer, U. 1970, Sol. Phys., 15, 158
Titov, V. S., Priest, E. R., & Démoulin, P. 1993, A&A, 276, 564
Trujillo Bueno, J. E., Landi Degl'Innocenti, E., Collados, M., Merenda, L., & Manso Sainz, R. 2002, Nature, 415, 403